SIMULTANEOUS MEASUREMENT OF TEMPERATURE AND STRAIN WITH A BRAGG GRATING SENSOR IN POLARIZATION-MAINTAINING FIBER

Emanuele Casciaro
Department of Aerospace Science and Technology, Politecnico di Milano
Milan (MI), Italy

Diego Henriquet
Department of Aerospace Science and Technology, Politecnico di Milano
Milan (MI), Italy

Andrea Baldi
Leonardo Helicopters, Leonardo Company, Cascina Costa di Samarate (VA), Italy

Paolo Bettini
Department of Aerospace Science and Technology, Politecnico di Milano
Milan (MI), Italy

ABSTRACT

This study aims to develop a reliable technique that enables fiber optic sensors to decouple strain and temperature effects, making them viable for real-world industrial applications. While current solutions demonstrate promising results in laboratory settings, they often lack robustness for integration into operational environments. The proposed approach leverages Fiber Bragg Grating sensors inscribed in polarization-maintaining fibers. The birefringent nature of these fibers produces two distinct Bragg reflections along orthogonal polarization axes, enabling accurate thermo-mechanical separation with a single sensing element. A dedicated experimental setup was designed to calibrate and test the sensors under controlled thermal and mechanical loads. Finite element models were used to study optimal fiber orientation for integration into composite structures. Tests identified the 45° orientation of the optical fiber section relative to the composite material section as the most balanced configuration, minimizing the need for recalibration post-embedding. Preliminary experimental results and simulations indicate that this type of sensors can reliably discriminate between thermal and mechanical influences. Future works include further data analysis to improve the sensing system's resolution and the development of more detailed models based on the Finite Element Method, supported by additional experimental validations.

NOTATION

*

Symbols

d Fiber Diameter, mm

E Young's modulus, GPa

F Force, N

α Coefficient of Thermal Expansion, $1/°C$

μ Friction Coefficient, $-$

ν Poisson's Coefficient, $-$

ξ Thermo-optic Coefficient, $1/°C$

ϕ Wrap Angle, rad

K_T Temperature Sensitivity Coefficient, $pm/°C$

K_ε Strain Sensitivity Coefficient, $pm/\mu\varepsilon$

l_0 Rest Length, mm

p_e Effective Photo-elastic Coefficient, $-$

ΔT Temperature Variation, $°C$

Δl Length Variation, mm

$\Delta\varepsilon$ Strain Variation, $\mu\varepsilon$

$\delta\lambda$ Difference between Slow and Fast Peak, nm

λ_B Bragg's Wavelenght, nm

*

Acronyms

ASA Acrylonitrile Styrene Acrylate

CTE Coefficients of Thermal Expansion

DCF Double-Cladding Fiber

DMF Dual-Mode Fiber

EPS Expanded Polystyrene

FBG Fiber Bragg Grating

FEM Finite Element Method

LPG Long-Period Grating

MK2 FBG in AtGrating Panda Fiber

MK3-S1 1^{st} FBG in FBGS Bow-tie Fiber

MK3-S2 2^{nd} FBG in FBGS Bow-tie Fiber

MTS Material Test System

ODB Output DataBase

PDL Polarization-Dependent Loss

PID Proportional-Integral-Derivative

PM Polarization-Maintaining

SAP Stress-Applying Parts

SEM Scanning Electron Microscopy

SHM Structural Health Monitoring

SMF Single-Mode Fiber

SQP Sequential Quadratic Programming

TRL Technology Readiness Level

XPS Extruded Polystyrene

INTRODUCTION

The structural health monitoring (SHM) of aeronautical components has emerged as a strategic priority in aerospace engineering, where safety-critical structures are subject to demanding operational conditions and require frequent inspections. Conventional maintenance strategies typically involve time-consuming and costly disassembly of components to verify structural integrity. Consequently, the development of onboard SHM systems capable of providing real-time diagnostics is highly desirable for improving safety, reducing downtime and optimizing maintenance costs.

Among the most promising technologies for SHM there are fiber optic sensors, which offer high sensitivity, immunity to electromagnetic interference, compact size and compatibility with embedding in composite materials. Their ability to function under harsh environmental conditions makes them particularly attractive for aerospace applications (Refs. 1,2).

In particular, Fiber Bragg Grating (FBG) sensors have been widely studied due to their multiplexing capabilities and spectral encoding of physical quantities such as strain and temperature. Their high Technology Readiness Level (TRL), along with their advanced development and proven reliability, makes them particularly suitable for industrial applications. These devices exploit the periodic modulation of the refractive index within the core of an optical fiber, which reflects specific wavelengths of light in accordance with Bragg's law. The reflected wavelength in FBG sensors is inherently sensitive to both strain and temperature variations, making them well-suited for high-resolution, real-time monitoring in environments where minimal invasiveness is critical (Refs. 3,4).

Despite their advantages, a major limitation of conventional FBG sensors is their inability to decouple mechanical and thermal effects from a single measurement. Since both strain and temperature influence the Bragg wavelength, a single FBG sensor cannot distinguish between the two effects without auxiliary information. This phenomenon, known as thermo-mechanical coupling, has been extensively investigated, prompting researchers to explore strategies for decoupling the two influences.

The most established method is the capillary technique, which consists of embedding two closely spaced fiber Bragg grating sensors (FBGs), one directly bonded to the host structure to measure mechanical strain and the other mechanically isolated, typically via a capillary tube, to respond exclusively to temperature variations. While this dual-sensor approach enables effective decoupling of strain and temperature effects, it introduces significant drawbacks. Specifically, it requires fiber interruption and mechanical discontinuities, which prevent the use of wavelength multiplexing and increase intrusiveness, particularly critical for composite structures and embedded sensor configurations (Refs. 5,6).

Other solutions involve more advanced fiber designs. A notable solution is proposed by Triollet et al. (Ref. 7), where a long-period grating (LPG) is superimposed with an FBG within the same fiber segment. By introducing a dedicated performance metric, the discrimination efficiency, the authors quantitatively evaluate the decoupling effectiveness. Their sensor achieves a discrimination efficiency of 99%, with measurement accuracies of $\pm 0.4\,^{\circ}$C for temperature and $\pm 5\,\mu\varepsilon$ for strain. The sensor also maintains performance after embedding in a metallic specimen, confirming its robustness. This metric is adopted in the present work to assess the proposed solution.

In another study, Hu et al. (Ref. 8) report the development of a hybrid FBG at the splice between a single-mode fiber (SMF) and a double-cladding fiber (DCF), using excimer laser inscription. The resulting device exhibits two distinct resonance dips with different strain and temperature sensitivities, enabling decoupled parameter retrieval via a simple two-variable matrix. The reported sensitivities are 12.3 and 13.2 pm/°C for temperature, and 0.69 and 0.76 pm/$\mu\varepsilon$ for strain, with root mean square errors of $\pm 1.6\,^{\circ}$C and $\pm 26.7\,\mu\varepsilon$, respectively.

Kang et al. (Ref. 9) propose a dual-parameter sensing system based on a twin-core fiber integrated into an erbium-doped fiber ring laser cavity. Identical FBGs are written into each core, generating two laser lines with distinct sensitivities. Decoupling is achieved by solving a linear system based on the wavelength shifts of the lasing peaks. Sensitivities are reported as $0.0092\,\mathrm{nm}/^{\circ}\mathrm{C}$ and $0.0116\,\mathrm{nm}/\mu\varepsilon$ for one core, and $0.0143\,\mathrm{nm}/^{\circ}\mathrm{C}$ and $0.0087\,\mathrm{nm}/\mu\varepsilon$ for the other. This laser-based configuration offers high resolution and low noise, benefiting from the narrow linewidths of the lasing signals.

Jiang et al. (Ref. 10) present a method involving FBG inscription in a dual-mode fiber (DMF) via femtosecond laser writing. The grating supports two core modes (LP_{01}, LP_{11}) along with cladding-mode resonances. A sensitivity matrix is constructed based on the shifts of the two Bragg peaks, enabling decoupled strain and temperature measurements. The sensor achieves high resolutions of approximately $\pm 6.3\,\mu\varepsilon$ and $\pm 0.8\,^{\circ}C$, proving effective for compact and multi-parameter sensing.

Finally, Pereira et al. (Ref. 11) present a method for in situ strain and temperature measurement by embedding a pair of FBGs into polymeric tensile specimens via injection molding. This approach enables strong mechanical coupling without surface bonding and enables independent monitoring of strain and temperature through angularly misaligned FBGs. The sensors exhibit identical responses to thermal variations and distinct responses to mechanical loading, enabling decoupling via a two-variable analytical model. Calibration showed a significant increase in thermal sensitivity upon embedding, due to the high thermal expansion coefficient of the polymer matrix. The method demonstrated high accuracy with less than 1% calibration error and proved suitable for combined thermal-mechanical loading scenarios in polymeric materials.

Alternative approaches to strain-temperature discrimination leverage the unique optical properties of specialized fibers, particularly polarization-maintaining (PM) fibers. In such fibers, inherent birefringence, originating from structural asymmetries or stress-induced anisotropy, induces distinct propagation constants for orthogonal polarization modes. This birefringence enables the separation of thermal and mechanical effects when properly exploited in sensing architectures.

Among the class of birefringent fiber sensors, fiber Bragg gratings (FBGs) inscribed in PM fibers represent a powerful tool for dual-parameter sensing. When an FBG is written into a PM fiber, it produces two distinct reflection peaks corresponding to the fast and slow polarization axes. The differential behavior of these peaks under strain and temperature variations allows the formulation of a linear system that enables the decoupling of these two quantities.

Wang et al. (Ref. 12) demonstrate this approach by implementing a polarization-maintaining few-mode fiber Bragg grating for simultaneous measurement of temperature and strain. The sensor utilizes both wavelength shifts and phase variations from two Bragg peaks associated with the even LP_{11} mode. Reported sensitivities include 10 pm/°C and -3.2 (10^{-2}) rad/°C for temperature (wavelength and phase, respectively), and $0.73\,\mathrm{pm}/\mu\varepsilon$ and $4\,(10^{-4})\,\mathrm{rad}/\mu\varepsilon$ for strain. A discrimination efficiency of 98% is achieved, indicating effective decoupling.

In a separate study, Oh et al. (Ref. 13) introduce a technique for decoupled sensing using a single FBG under stress-induced birefringence and polarization-dependent loss (PDL). Following femtosecond-laser inscription and mechanical loading, the FBG supports two polarization modes with different sensitivities. By monitoring both the Bragg wavelength shifts and PDL variations, the authors demonstrate reliable decoupling of strain and temperature within a single grating element.

Several studies have demonstrated the feasibility of PM fiber-based FBG sensors for multi-parameter sensing. However, most of these investigations have been limited to ideal laboratory conditions. The behavior of such sensors when embedded into composite materials, where residual curing stresses, mechanical constraints, and anisotropic stiffness can significantly alter sensor response, remains largely underexplored.

The present study, building upon previous results (Refs. 14, 15), aims to enhance thermo-mechanical decoupling in PM-FBG sensors and to evaluate their performance when embedded in composite materials. The approach relies on the dual-peak response inherent to these gratings, with the fast-axis Bragg wavelength shift and the inter-peak spacing providing distinct sensitivities to strain and temperature. This enables dual-parameter extraction from a single sensing element, thereby minimizing invasiveness and reducing the likelihood of fiber damage when integrated into host structures.

Thermo-mechanical decoupling was achieved after the calibration process. The developed calibration setup enabled extended testing under variable thermal and mechanical loads. The resulting discrimination efficiency of approximately 10% aligns with comparable studies in the literature, demonstrating the feasibility of achieving reasonable decoupling performance even with only two measurement parameters. While this level of discrimination may appear modest, it is considered effective in light of the reduced sensor complexity and its potential for embedded applications. Under optimal loading and temperature conditions, the best-performing sensor yielded residuals with a mean and standard deviation of $-0.55 \pm 9.48\,^{\circ}\mathrm{C}$ for temperature and $-12.68 \pm 97.20\,\mu\varepsilon$ for strain.

Given the relevance of embedded sensing in aeronautical applications and composite materials, the orientation of the fiber within the host laminate was identified as a critical factor influencing sensor behavior. The embedment of PM fiber may lead to calibration shifts, depending on the fiber's cross-section orientation. To address this, a finite element model based on stress-induced birefringence was developed and validated against experimental results. The model accurately reproduced the observed sensitivity trends and confirmed that effective decoupling remains achievable post-embedding, provided the fiber is oriented at approximately 45° with respect to the laminate thickness direction. In contrast, suboptimal orientations led to degradation in sensitivity and discrimination, necessitating a full recalibration. These findings emphasize the importance of both precise fiber orientation and robust modeling to ensure reliable dual-parameter sensing in real-world composite structures.

The *Materials and Methods* section details the methodology used to extract strain and temperature information from PM-FBG sensors. It also describes the custom experimental setup developed specifically for birefringent fiber interrogation. Importantly, the setup maintains compatibility with standard FBG sensors and other sensors of comparable geometry. Comprehensive information regarding the fiber types and sensor specifications employed in the study is also provided.

The *Calibration and Testing* subsection outlines the mechanical and thermal calibration protocols, as well as mixed loading tests conducted to validate sensor performance. The corresponding experimental data are presented and analyzed in the *Results – Calibration and Testing* section.

The *Numerical Model* subsection introduces finite element simulations designed to quantify the influence of fiber cross-sectional orientation once embedded in composite laminates. The outcomes of these simulations are discussed in the *Results – Numerical Model* section.

The *Experimental Validation and Testing* subsection describes the embedding campaign in which sensors were integrated at various angular orientations. The effects of embedding on sensitivity were assessed, followed by post-embedding recalibration. Fiber orientation within the host matrix was verified using scanning electron microscopy (SEM). The findings are reported in the *Results – Experimental Validation and Testing* section.

A critical analysis of the overall results is presented in the *Discussion* section, which also identifies limitations and future development opportunities. Finally, the *Conclusions* section summarizes the key findings and contributions of the study. Taken together, the results offer meaningful insight into the practical use of PM-FBG sensors and their integration in aerospace-grade composite structures.

MATERIALS AND METHODS

FBGs Measurement System

In the case of a single standard FBG sensor, both mechanical strain and temperature contribute to the shift in Bragg wavelength. A common analytical approach involves expressing the wavelength shift as a linear combination of these two effects (Ref. 16):

$$\Delta\lambda_B = \lambda_B[(1-p_e)\,\Delta\varepsilon + (\alpha+\xi)\Delta T]\,, \tag{1}$$

where λ_B is the initial Bragg wavelength, $\Delta\varepsilon$ is the applied axial strain, ΔT is the temperature change, p_e is the effective photo-elastic coefficient, α is the thermal expansion coefficient of the fiber and ξ is the thermo-optic coefficient of the core material. This linearized expression is derived from the combined effects of the elasto-optic, thermo-optic and thermal expansion phenomena inherent to the optical fiber. While it provides a good first-order approximation, in practical applications the inability to decouple $\Delta\varepsilon$ and ΔT from a single measurement limits the accuracy of multi-physics sensing with a single FBG sensor.

A common analytical approach involves the use of two closely spaced FBG sensors, under the assumption that both are subjected to the same temperature and strain conditions. This enables the formulation of a system of two equations with two unknowns, from which the strain and temperature can be independently determined. However, this method requires specific design strategies to ensure that the two sensors exhibit sufficiently different sensitivities, thereby enabling effective thermo-mechanical decoupling.

The strategy involving the use of a single FBG sensor inscribed in a birefringent fiber enables the formulation of two equations similar to Eq. 1, but with distinct sensitivity coefficients. Birefringent optical fibers operate by introducing a controlled difference in the refractive indices along two orthogonal axes of the fiber core. As a result, light polarized along these axes propagates at different phase velocities, giving rise to a well-defined birefringence. When FBGs are inscribed into these fibers, this birefringence manifests as a spectral splitting of the Bragg peak into two distinct components, corresponding to the fast and slow polarization axes. The behavior of these peaks under varying temperature or strain conditions enables the decoupling of thermal and mechanical effects, as the two polarization modes (associated with the fast and slow peaks) exhibit different sensitivities to external perturbations (Eq. 2):

$$\begin{cases}\Delta\lambda_{fast} = K_\varepsilon^{fast}\cdot\Delta\varepsilon + K_T^{fast}\cdot\Delta T\\ \Delta\lambda_{slow} = K_\varepsilon^{slow}\cdot\Delta\varepsilon + K_T^{slow}\cdot\Delta T\,,\end{cases} \tag{2}$$

where $\Delta\lambda$ denotes the wavelength shift, K_ε represents the strain sensitivity coefficient and K_T is the temperature sensitivity coefficient. In particular, this work considers two equations: one corresponding to the fast axis response, and the other related to the wavelength separation ($\delta\lambda$) between the two birefringent peaks (Eq. 3) (Ref. 15).

$$\begin{cases}\Delta\lambda_{fast} = K_\varepsilon^{fast}\cdot\Delta\varepsilon + K_T^{fast}\cdot\Delta T\\ \Delta(\delta\lambda) = K_\varepsilon^{diff}\cdot\Delta\varepsilon + K_T^{diff}\cdot\Delta T\,.\end{cases} \tag{3}$$

This resolution scheme yields improved results due to the presence of distinct sensitivity coefficients, one of which is negative. This behavior is attributed to the opposite shifts of the fast and slow peaks. They move closer together as temperature increases and further apart as strain increases. Consequently, the calibration lines of the two peaks are not parallel, reflecting their differing sensitivities to strain and temperature.

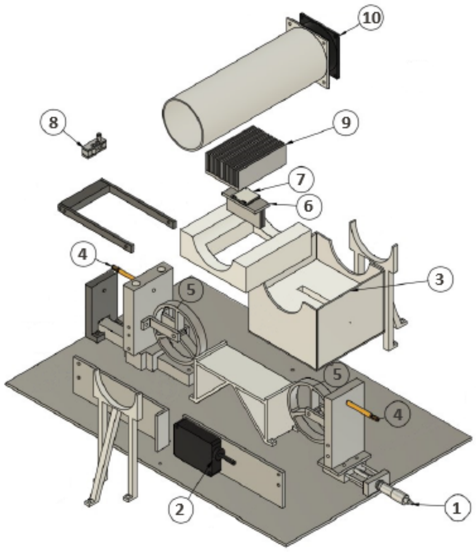

Figure 1. Experimental setup developed for calibration and testing of optical fibers. (1) Micrometric slide. (2) Laser displacement sensor NipponAutomation LAS-8010V. (3) Thermal chamber. (4) Newport FPH-J fiber chucks. (5) Capstans. (6) Internal heat sink. (7) Peltier cell Adaptive ETH1271013SHI. (8) Load cell Futek LRF300. (9) External heat sink for cooling by forced-air convection within the duct. (10) Fan RsPro 7033442 for generating forced-air convection.

Experimental Setup

An experimental setup was designed to apply both mechanical and thermal stimuli (Figure 1). The apparatus was designed to ensure high measurement precision, enable wide temperature range operation, and prevent fiber failure under mechanical strain. The design of the experimental setup focused on two critical aspects: thermal control and mechanical clamping. These were optimized to improve the accuracy of fiber optic sensor calibration, enable testing at sub-ambient temperatures and increase the strain range without compromising fiber integrity.

The thermal control subsystem employs a Peltier element governed by a Proportional-Integral-Derivative (PID) controller. The use of both internal and external aluminum heat sinks enhances thermal exchange efficiency. For mechanical clamping, Newport FPH-J fiber chucks are combined with a capstan-based mechanism. The capstan reduces the load transferred to the chucks by exploiting friction between the fiber and the capstan surface, thereby minimizing the risk of slippage and fracture. The load reduction follows the Euler–Eytelwein relationship (Ref. 17):

$$F_{load} = F_{transmitted}\, e^{\mu \phi} \ , \tag{4}$$

where F_{load} and $F_{transmitted}$ are the axial loads in the fiber before and after the capstan, respectively. μ is the friction coefficient, while ϕ is the wrap angle in radians of the optical fiber on the capstan. The load cell has a maximum capacity of 44 N and an accuracy of 0.1761 N. The thermal chamber is made of acrylonitrile styrene acrylate (ASA) and filled with glass wool insulator to ensure thermal insulation and stability. Other materials were also considered as insulators, such as expanded polystyrene (EPS) and extruded polystyrene (XPS), but glass wool was ultimately selected due to its wider operational temperature range, especially since EPS and XPS begin to decompose around 75 $°C$, a temperature lower than the planned testing conditions. The fan used for generating the airflow inside the wind tunnel provides an airflow of 0.047 m^3/s and a maximum static pressure of 201.6 Pa.

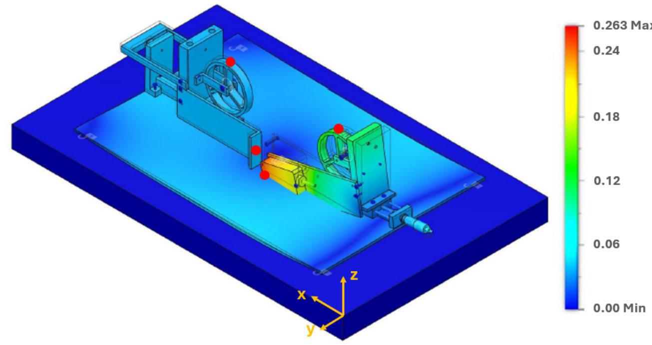

Figure 2. Mechanical analysis of global displacements using finite element model. Result was magnified to highlight details.

Static structural analyses in FUSION were conducted using finite element modeling to evaluate the mechanical deformation of the measurement setup and its impact on sensor readings (Figure 2). It was possible to determine which components could be made of aluminum and which ones required steel. Solid elements were used, with a total of 118357 nodes and 68745 elements. The simulation included a fixed idealized bench supporting the setup, with non-penetration constraints at all contact interfaces. To block the in-plane rigid body motion of the support, the midpoint of the plate was fixed in the x- and y-directions and the corners of the plate in the y-direction. The elements in blue are the bolt connectors that link the different components of the model. They were considered to be made of aluminum. The analysis applied two opposing forces ($F = 20\ N$) at the capstans to replicate the fiber's reaction force during deformation.

Simulation results showed asymmetric deformation, with greater displacement on the side supported by the micrometric slide due to its lower stiffness compared to the steel guide rail. This led to differential movement between the capstans and between the laser and reflector positions (highlighted in red in Figure 2), potentially introducing measurement errors. The displacement of a fiber during deformation was calculated using the Eq. 5:

$$\Delta l = \frac{l_0\, F}{E\, \pi \frac{d^2}{4}} \ . \tag{5}$$

A rest length (l_0) of 285 mm between the two capstans was

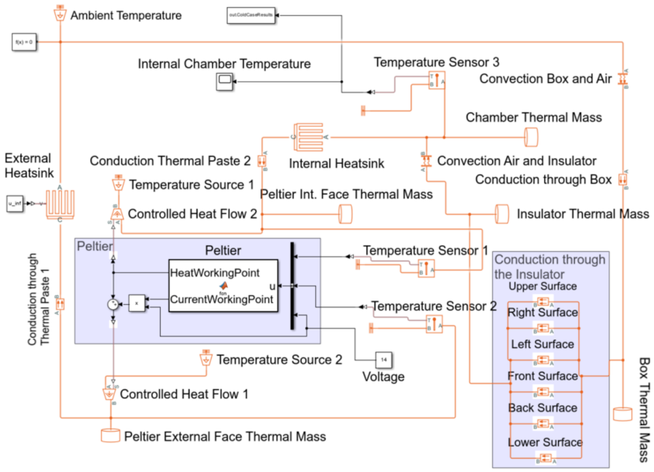

Figure 3. MATLAB Simulink model for thermal analysis used to evaluate effectiveness of the insulation system and cooling performance of Peltier cell. An analogous scheme was implemented for heating cycle.

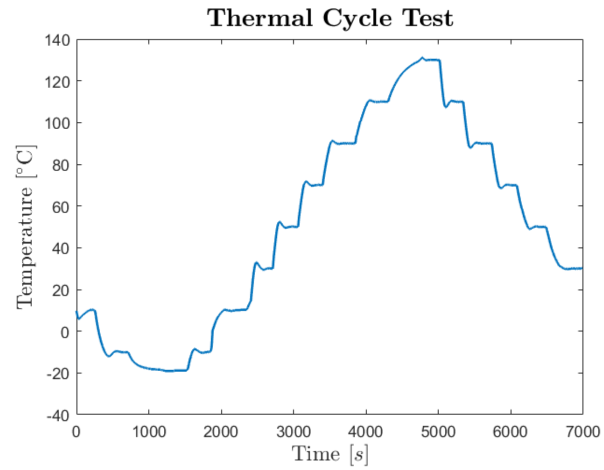

Figure 4. Thermal cycling test with PID controller.

considered. A Young's modulus (E) of 53 GPa and a fiber diameter (d) of 0.145 mm were obtained by averaging values reported in the literature. Under the applied forces, the fiber displacement was calculated to be 6.52 mm. From the numerical simulations, the displacement components were extracted at four critical points, showing relative displacements of 0.129 mm between the capstans and 0.234 mm between the laser and reflector. The resulting measurement error was estimated to be 0.105 mm, corresponding to a relative error of 1.61%, which remains below the intrinsic accuracy of the laser sensor ($\pm 150\ \mu m$), thus confirming the mechanical reliability of the setup for the intended mechanical calibration tasks.

A thermal model of the experimental system was developed in MATLAB Simulink to predict the achievable temperature range and evaluate the dynamic response during thermal cycling. The model (Figure 3) simulates the cooling phase, with a mirrored configuration used for heating. The system accounts for heat exchange with the external environment through both forced convection (via the external heat sink) and natural convection (through the outer surfaces of the box).

The model includes a detailed representation of the Peltier element. The hot and cold surfaces are thermally linked to their respective heat sinks via thermal paste. The Peltier block receives as input the temperatures at both surfaces and the applied voltage, from which it calculates the electrical current, the heat absorbed at the cold side and the heat expelled at the hot side. These calculations are based on interpolated manufacturer data sheets, which relate thermal behavior to electrical and thermal inputs. The cold side of the Peltier cools the internal radiator by conduction, which in turn cools the chamber air by natural convection. Heat exchange with the insulation and outer box is modeled through conduction. In heating mode, the heat flow is reversed by inverting the functional roles of the Peltier's hot and cold surfaces.

The thermal simulations predicted a minimum chamber temperature of -13.92 $°C$ during cooling and a maximum of 146.92 $°C$ during heating. To assess dynamic behavior, the time required to reach within 5% of the asymptotic temperatures was computed. For the cooling cycle, a temperature of $-13.22\ °C$ was reached in approximately 1556 s, while for the heating cycle, 139.57 $°C$ was reached in only 328 s. These results confirm the system's capability to operate over a wide and controllable thermal range.

A preliminary thermal test was performed without the optical fiber to validate the stability and accuracy of the thermal control subsystem. The chamber was subjected to a stepped thermal cycle starting from 10 $°C$, decreasing in 20 $°C$ increments to the system's lower limit, then increasing in similar increments to the upper limit, before returning to ambient temperature. At each temperature step, after enabling the system to stabilize, the temperature was recorded via thermocouple for 30 s to assess thermal stability. As shown in Figure 4, the PID controller produced a minor initial overshoot at each step, followed by stable temperature regulation.

The analysis of temperature fluctuations revealed standard deviations ranging from 0.003 $°C$ to 0.153 $°C$, with a mean of 0.071 $°C$, indicating high thermal stability. The experimentally achieved minimum and maximum temperatures were $-19.62\ °C$ and 131.58 $°C$, respectively. These results validate the thermal system's performance and confirm its suitability for accurate and repeatable thermo-mechanical calibration of fiber optic sensors.

A series of preliminary experiments were conducted to validate the precision of the mechanical calibration system using a single-mode optical fiber with an embedded FBG sensor. The inclusion of capstans in the clamping system serves to reduce the stress concentration at the fiber–chuck interface, thereby minimizing the risk of breakage and enabling the application of higher strain levels. During loading, the fiber remains firmly held by the capstans, enabling a consistent application of force. However, during unloading, the tension within the fiber decreases, leading to minor slippage around

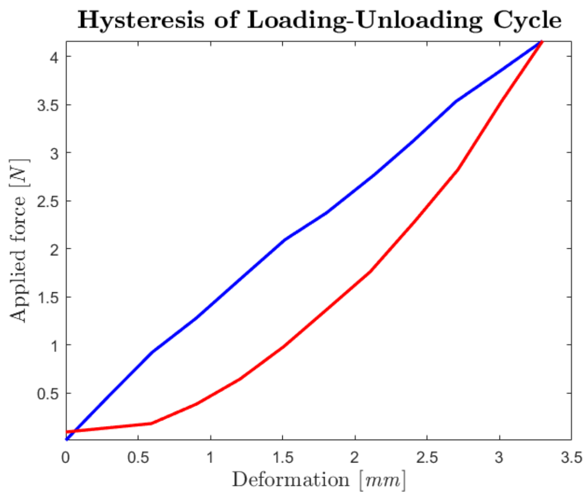

Figure 5. Mechanical deformation cycle exhibiting hysteresis due to use of capstans.

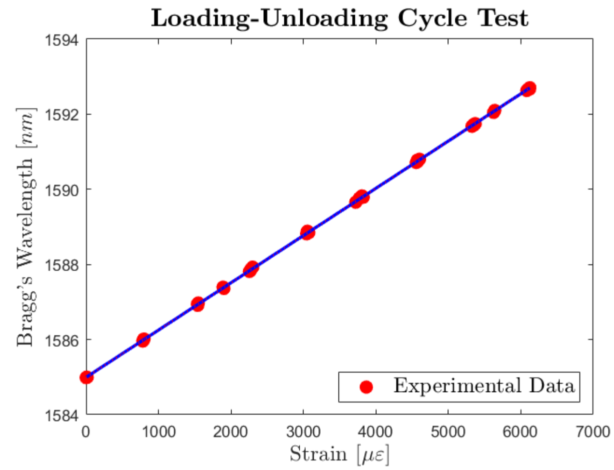

Figure 6. High-strain mechanical cycling test without hysteresis.

the capstans and resulting in a hysteresis effect. This behavior is clearly observed in the force–displacement curve shown in Figure 5, where unloading forces are systematically lower than loading forces for equivalent displacements. The displacement remains unaffected by slippage, as it is measured externally via the laser-reflector system, whereas the internal stress, and consequently the measured force, decreases. Hence, displacement cannot reliably be used to infer strain in the presence of capstan-induced hysteresis.

To address this, force measurements were used instead to compute fiber strain, as the load cell directly reflects the internal stress state of the fiber segment between the capstans. Using the linear relationship defined by Hooke's law, a force-to-strain proportionality constant was experimentally determined under low-strain, hysteresis-free conditions. These calibration tests were conducted without capstans to avoid slippage and repeated three times. Each calibration test involved a loading–unloading cycle, recording 11 static measurement points per cycle over 30 s. After each test, a linear fit was applied to extract the force–strain sensitivity and the final conversion parameter was obtained as a weighted average based on the adjusted R^2 of the fits.

This conversion factor enabled subsequent high-strain tests with capstans, bypassing the inaccuracies introduced by displacement measurements of the laser sensor. In these tests, both fiber strain and the Bragg wavelength shift of the FBG sensor were recorded under constant temperature conditions, ensuring that wavelength variation was solely due to mechanical strain. The results, shown in Figure 6, exhibit high linearity with an adjusted R^2 of 0.999 across all three test cycles, confirming the repeatability and precision of the calibration method and validating the mechanical sensitivity of the FBG sensor under high strain conditions.

From the experimental setup developed, it is therefore possible to apply thermal cycles (from $-19.62\ °C$ to $131.58\ °C$) with excellent temperature stability. Mechanical cycling highlighted the need for capstans to prevent fiber slippage. With these latest modifications, it was possible to achieve deformations in the sensor region of up to 8000 $\mu\varepsilon$.

Types of Fibers

Three fiber-optic sensors were calibrated. The first (MK2), produced by AtGrating, consists of a single sensor inscribed on a commercial acrylate-coated Panda fiber (Figure 7 left), which is cost-effective but offers limited performance due to its non-specialized design. The second (MK3-S1) and third sensors (MK3-S2), manufactured by FBGS, are part of a 15-sensor array inscribed on an Ormocer-coated Bow-Tie fiber (Figure 7 right), specifically engineered for sensing applications. Although more expensive, the Bow-Tie geometry provides enhanced birefringence, resulting in improved sensing performance.

Stress-induced birefringent fibers, such as Panda and Bow-tie types, achieve birefringence through asymmetrical stress regions integrated during the fabrication process. In Panda fibers, two cylindrical stress-applying parts (SAPs) are symmetrically placed on either side of the core. Bow-tie fibers, on the other hand, employ trapezoidal stress regions arranged diagonally relative to the core, achieving a similar effect through a different stress distribution geometry. This stress is primarily induced during the fiber cooling process by the mismatch in the coefficients of thermal expansion (CTE) and Poisson's ratio between the stress-applying elements and the surrounding cladding material, giving rise to the resulting birefringence (Refs. 18–20).

Figure 8 presents the nominal wavelengths of the three sensors measured at 30 $°C$ without applied strain. Measurements were averaged over 30 s and repeated three times for reliability. FBGS sensors showed wider peak spacing and higher birefringence than AtGrating sensors, which exhibited lower noise and required less amplification to reach the same optical power. The wavelength values from which the fiber birefringence can be evaluated are reported in Table 1.

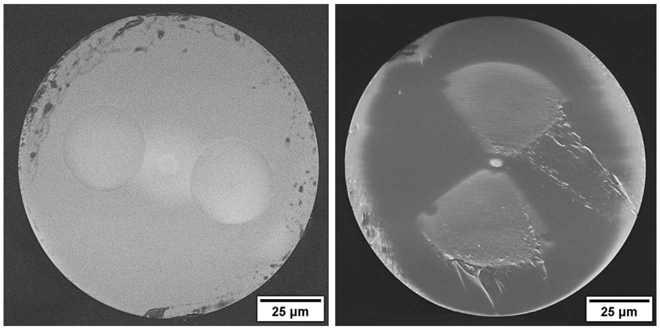

Figure 7. Panda-type (left) and Bow-tie (right) polarization-maintaining optical fibers.

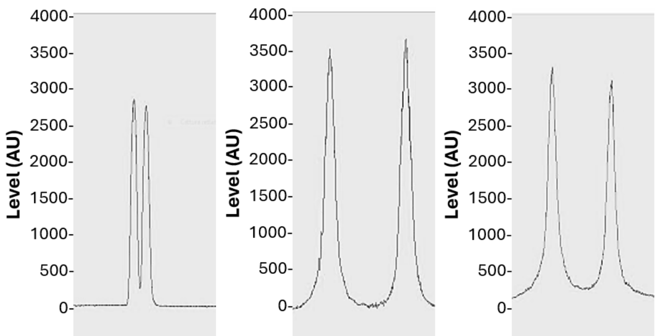

Figure 8. Peaks of FBG sensors: MK2 in Panda-type fiber (left), MK3-S1 in Bow-tie fiber (center) and MK3-S2 in Bow-tie fiber (right).

Calibration and Testing

The first phase of the study focused on calibrating the FBG sensors to determine their temperature and strain sensitivity coefficients. Initial tests were conducted under low-strain conditions ($\sim 2000\ \mu\varepsilon$) without capstans to derive the force-to-wavelength conversion coefficient. Each test involved a loading–unloading cycle repeated three times, with 11 static data points recorded for 30 s per cycle. Fitting coefficients were calculated for each trial, and a final value was obtained as the weighted average based on the adjusted R^2.

Subsequently, high-strain tests were performed using capstans to evaluate the reflected wavelength shifts at elevated strain levels. For the AtGrating fiber, strain was increased up to 8100 $\mu\varepsilon$ (80% of the specified fiber limit), while the FBGS fiber was tested within the 5% maximum strain limit. Practical strain limits for the first and second sensors, 6000 $\mu\varepsilon$ and 2500 $\mu\varepsilon$ respectively, were imposed to prevent spectral peak overlap within the sensor chain. Although cutting the fiber into individual sensors could have resolved this, it was decided to maintain the full chain to assess how the calibration range influences accuracy. Strain-sensitivity calibration was repeated three times, each with a load–unload cycle, and eight static points were recorded per cycle over 30 s, followed by time-averaged data processing.

Thermal sensitivity was evaluated through three additional tests conducted under zero-strain conditions. Temperature was varied from -10 °C to 100 °C in 10 °C increments to assess its effect on the fast peak wavelength and peak spacing. Each test included a full heating and cooling cycle. At each temperature point, a 4 min stabilization period was applied after first reaching the target temperature to mitigate PID-induced oscillations and ensure steady-state conditions. Subsequently, signals were recorded for 30 s and time-averaged values were used for analysis.

Table 1. Nominal wavelengths of FBG sensors in birefringent fibers.

	λ_{fast} $[nm]$	λ_{slow} $[nm]$	$\delta\lambda$ $[nm]$
MK2	1549.801	1550.146	0.3449
MK3-S1	1514.992	1515.795	0.8033
MK3-S2	1519.768	1520.560	0.7921

Following the sensor calibration phase, tests under combined conditions were performed. One test involved varying the temperature while maintaining constant strain, and two tests were conducted at constant temperature with varying strain. These experiments enabled the evaluation of the system's ability to decouple the thermal and mechanical contributions.

Numerical Model

The second phase of the research focused on evaluating changes in sensor performance, specifically thermal and mechanical sensitivity, following their embedding into composite materials. This assessment is critical to determine the feasibility of applying this sensing technology in aeronautical structures by integrating the sensors within composite components.

Notably, the orientation of the fiber cross-section relative to the thickness direction in the composite cross-section may alter the stress state on the fiber during the autoclave curing process, which in turn can influence the stress-induced birefringence (Figure 9). To investigate this, a Digital Twin model of the fiber was developed to simulate its behavior both before and after embedding into composite specimens.

To simulate the stress-induced birefringence generated during fiber manufacturing, a cooling cycle from 1000 °C to 30 °C was modeled, reflecting the temperature range at which birefringence typically develops during the fiber drawing process. This enabled the reconstruction of the residual stress distribution responsible for birefringence. The model was initially validated against data from the literature (Ref. 21). Subsequently, it was refined using the actual fiber geometry obtained via scanning electron microscopy (SEM), where the core, cladding and stress-applying parts (SAPs) were clearly identified. The coating was removed prior to imaging, and its diameter (180 μm) was measured separately. The measured dimensions are shown in Table 2.

The ABAQUS model (Figure 10) consists of 235157 nodes and 202240 elements, including 201040 linear hexahedral elements of type C3D8R and 1200 linear wedge elements of type C3D6. The mesh quality of the model is well suited for the intended analysis. The core region shows good mesh characteristics, with no elements exceeding an aspect ratio of 10 and a maximum value of 6.64. Other structurally relevant parts, such as SAPs, present high-quality meshes with low aspect ratios and no distortion. The cladding, while containing a small percentage of hex elements with aspect ratios above 10 (5.98%) and a worst case of 17.00, does not significantly affect the optical behavior of the core. Given that the goal of this study is to observe the qualitative trend of birefringence as a function of stress rather than obtaining exact numerical values, the current mesh is sufficiently accurate for the analysis. The core and SAPs are bound to the cladding by tie-constraint. The step is divided into two static, general parts linked to a predefined initial and final temperature field.

Three simulations were conducted. The first computed the residual stresses due to thermal contraction from the fictive temperature down to room temperature. The resulting stress field was then transferred to two subsequent simulations: one for mechanical loading and one for thermal variation. In the mechanical case, axial displacement boundary conditions were applied to induce a 2% strain. In the thermal case, the temperature was increased from 30 $°C$ to 130 $°C$. From these simulations, the σ_{11} and σ_{22} stress components at the fiber core were extracted, as these two quantities are related to each other through the relative stress-photoelastic coefficient, that for polarization maintaining optical fiber is equal to 3.4305 (10^{-12}) m^2/N (Ref. 18). Knowing the difference between the refractive indices and the grating pitch, experimentally measured as 536.6951 nm, the peak separation was calculated under various temperature and strain conditions using Bragg's equation. By interpolating the resulting trends, the strain and temperature sensitivities of the fiber peak separation were determined.

Strain and thermal sensitivities were initially compared to experimental data, yielding relative errors of 28.25% and 46.51%, respectively. Additional validation parameters, such as peak separation at 30 $°C$ and Young's modulus, exhibited even larger discrepancies, with relative errors of 98.53% and 56.85%. These deviations were primarily attributed to uncertainties in the material property data used in the initial model.

To enhance the accuracy of the Digital Twin, an optimization procedure was implemented using MATLAB in conjunction with ABAQUS. Five key parameters were selected for optimization: the Young's modulus, Poisson's ratio and thermal expansion coefficient of the SAPs, along with the mechanical properties of the cladding and core materials. The ABAQUS input files were parametrized and automatically updated through MATLAB scripts and simulation results were extracted from the corresponding ODB files.

A nonlinear constrained optimization was then carried out using MATLAB's fmincon function with the Sequential Quadratic Programming (SQP) algorithm. The objective function, defined as the sum of relative errors between simulated and experimental values, was minimized with respect to five decision variables under simple bound constraints (Table 3).

The optimized model demonstrated substantial improve-

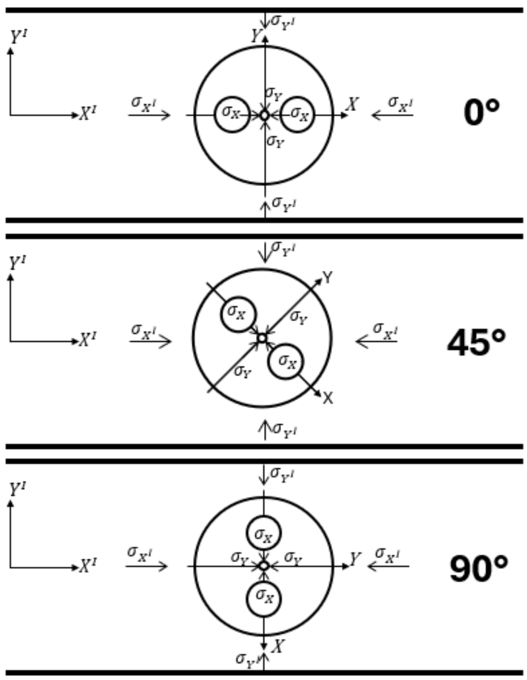

Figure 9. Different orientations of the PM optical fiber cross-section considered after embedding into composite material specimens. y' direction corresponds to thickness direction of composite specimens.

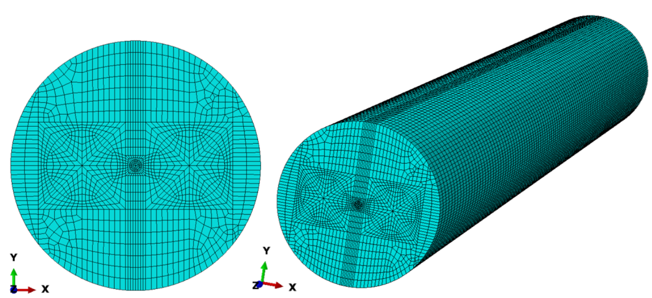

Figure 10. ABAQUS model of Panda-type optical fiber. Mesh details.

Table 2. Geometric parameters related to cross-section of Panda-type PM optical fiber.

	Size $[\mu m]$
Caldding diameter	122
SAP diameter	34.375
Core diameter	7.5
SAP-center distance	27.15
Coating diameter	180

Table 3. Upper and lower boundary values considered for optimization algorithm.

	Lower	Upper
E_{SAP} $[MPa]$	30000	33000
ν_{SAP} $[-]$	0.17	0.3
CTE_{SAP} $[1/°C]$	0.56 (10^{-6})	3.44 (10^{-6})
E_{core} $[MPa]$	40000	48000
$E_{cladding}$ $[MPa]$	40000	50000

Table 4. Mechanical properties of unidirectional glass fiber-reinforced composite with respect to globular reference system. Direction *z* is parallel to optical fiber while direction *x* is perpendicular to optical fiber.

E_z $[MPa]$	45700
E_x $[MPa]$	13500
ν $[-]$	0.27
CTE_z $[1/°C]$	2 (10^{-6})
CTE_x $[1/°C]$	20 (10^{-6})

ments, reducing the relative errors in Young's modulus, peak separation, thermal sensitivity and strain sensitivity to 0.11%, 17.37%, 13.31%, and 0.02%, respectively.

Following the calibration of the fiber model, composite panels were developed to investigate the influence of sensor embedment on sensitivity (Figure 11). The designed panel had a frontal cross-section of 25 mm × 2.5 mm and a thickness of 1 mm. The geometry was modeled as a 3D deformable solid and partitioned to improve meshing control. Material properties for the unidirectional glass fiber-reinforced composite were applied using an anisotropic formulation aligned with the global coordinate system (Table 4).

A surface-to-surface tie constraint was implemented to model the interaction between the fiber and composite, assigning the composite as the master surface due to its higher stiffness. The mesh employed C3D8R hexahedral elements, with refinement concentrated in the central region to accurately capture the interaction behavior while reducing mesh density elsewhere to manage computational cost. The final model consisted of 229221 nodes and 184648 elements. The mesh quality of the model is generally adequate for the purpose of this study. The core region, which is the most critical for evaluating stress-induced birefringence, is well meshed, with no elements exceeding an aspect ratio of 10 and a maximum aspect ratio of 5.31. Other regions such as coating and SAPs also exhibit good mesh quality. While parts like cladding and composite regions show a higher proportion of elements with poor aspect ratios, these areas are peripheral to the optical core and do not significantly influence the birefringence behavior of interest. Since the objective is to capture the qualitative trend of birefringence with respect to applied stress and not to compute exact quantitative values, the current mesh resolution is considered sufficient and appropriate.

Six simulations were conducted to evaluate the thermo-mechanical response of the embedded sensor, considering three fiber orientations relative to the composite: 0°, 45° and

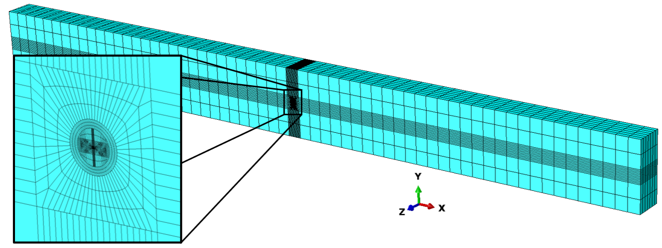

Figure 11. ABAQUS model of Panda-type optical fiber. Mesh details.

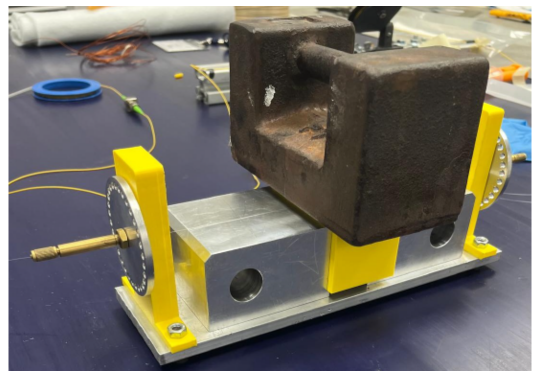

Figure 12. Experimental setup for controlling cross-sectional orientation of optical fiber relative to composite laminate during embedment process.

90°. In each case, residual stresses from the fiber cooling simulation were imported as initial conditions. Mechanical loading involved an applied strain of 2%, while thermal loading spanned a temperature range from 30 $°C$ to 130 $°C$. Stresses at the central node of the fiber core were extracted and used to compute updated thermal and mechanical sensitivity trends.

Experimental Validation and Testing

To experimentally validate the sensitivity variations observed in the numerical simulations, the three sensors were embedded into unidirectional glass fiber-reinforced composite specimens. A dedicated experimental setup was developed to control and assess the fiber cross-sectional orientation during embedment. The setup included two rotating wheels for chuck alignment, a metallic base in contact with the fiber and a U-shaped support for uniform load distribution (Figure 12). The method exploited the birefringence behavior of PM fibers under lateral stress: when the applied force (working through a weight) acts at 45° with respect to the fast and slow axes, the induced birefringence is minimized due to symmetric axial components. This condition was monitored using an FBG interrogator by tracking the peak separation in the reflected spectrum. Once a stable peak distance was observed, the fiber orientation was identified, enabling further rotations to determine the 0° and 90° configurations.

Following this procedure, three sensors were embedded at distinct orientations with respect to the composite global reference frame: the first FBGS (Bow-tie) at 45°, the second

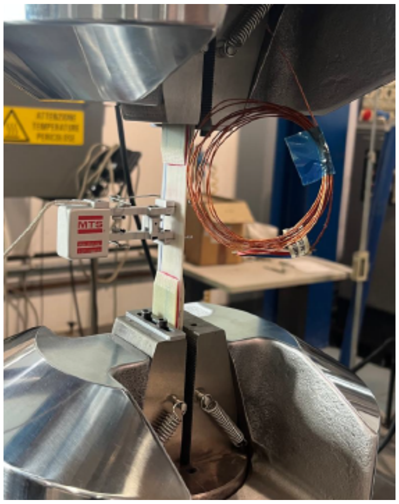

Figure 13. MTS 810 Material Test System used to calibrate and test composite specimens with embedded PM fiber-based FBG sensors.

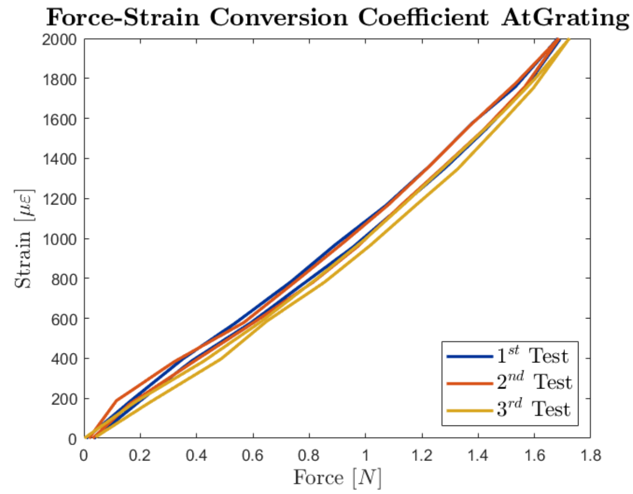

Figure 14. Test to determine force–strain conversion factor at low load levels for AtGrating fiber.

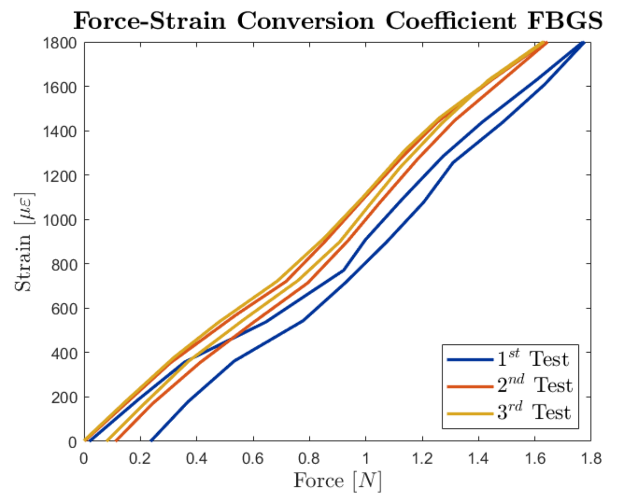

Figure 15. Test to determine force–strain conversion factor at low load levels for FBGS fibers.

FBGS (Bow-tie) at 0° and the AtGrating (Panda-type) at 90°. Each sensor was co-located within a few millimeters of a thermocouple to capture local temperature during calibration and testing. The composite specimens were cured in an autoclave at 125 $^{\circ}C$ for 1 h.

Post-embedment, the sensors were re-calibrated. Mechanical calibration was performed using an MTS 810 Material Test System equipped with an MTS 634.31F-24 strain gauge adhered to the specimen surface (Figure 13). Thermal calibration for the AtGrating and the first FBGS sensor was conducted in a Memmert Universal Oven UF110plus. Throughout the FBG sensor data acquisition campaign, the sm130 Micron Optics Optical Sensing interrogator was employed for signal interrogation and data collection. The same device was employed during the tests on unembedded fibers.

To assess combined thermo-mechanical response, additional tests were performed by simultaneously applying mechanical strain (via the MTS system) and temperature variations using infrared lamps. Finally, the specimens were sectioned, polished and analyzed with SEM to verify the actual sensor orientation within the composite structure.

RESULTS

Calibration and Testing

During the calibration phase, strain values were indirectly computed from force measurements obtained using a load cell, selected due to its lower susceptibility to hysteresis compared to alternative sensing methods. To enable this approach, a force-to-strain conversion factor was first established. All tests were carried out under controlled thermal conditions, maintaining the temperature at the nominal value of 30 $^{\circ}C$ (Figure 14 and 15).

Knowing the gauge length (i.e., the distance between chucks) and using displacement measurements acquired via laser sensors, accurate strain values were calculated. These values, unaffected by the hysteresis typically introduced by capstans, were then correlated with the load cell data to determine the conversion coefficient at low strain levels (Table 5).

As observed, the standard deviation is significantly smaller than the nominal value, which can be considered as evidence of the reliability and accuracy of the low-strain calibration procedure carried out.

Once the conversion coefficient was defined, capstans were installed to enable the application of higher strain levels and the corresponding measurement of wavelength shifts. This allowed for mechanical calibration over a broader strain range.

Table 5. Force–strain conversion coefficients (mean and standard deviation) for AtGrating and FBGS fibers.

$K_{AtGrating}$ [$\mu\varepsilon/N$]	1158.22 ± 4.5
K_{FBGS} [$\mu\varepsilon/N$]	1131.22 ± 52.2

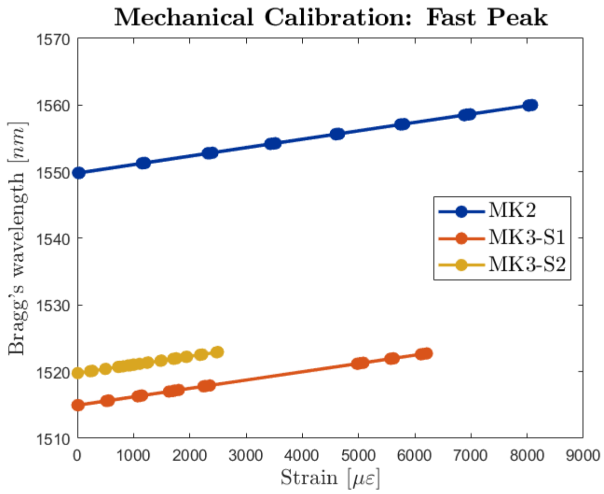

Figure 16. Mechanical calibration of AtGrating fiber sensor (MK2) and FBGS fiber sensors (MK3-S1 and MK3-S2). Different maximum strain values due to management of sensor chain for the two FBGs on FBGS fiber.

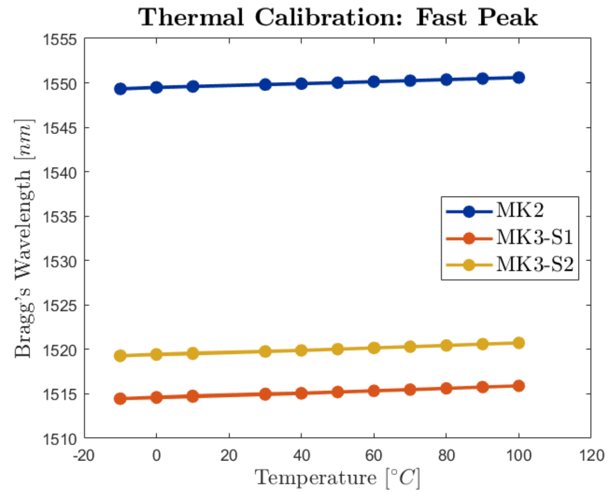

Figure 17. Thermal calibration of AtGrating fiber sensor (MK2) and FBGS fiber sensors (MK3-S1 and MK3-S2).

Table 6. Mechanical and thermal sensitivity of fast peak and peak separation for FBG inscribed in Panda birefringent fiber by AtGrating (MK2), FBG in Bow-tie birefringent fiber by FBGS (MK3-S1) and FBG in Bow-tie birefringent fiber by FBGS (MK3-S2).

	MK2	MK3-S1	MK3-S2
K_{ε}^{fast} $[pm/\mu\varepsilon]$	1.264	1.250	1.265
K_{T}^{fast} $[pm/°C]$	11.292	12.88	13.03
K_{ε}^{diff} $[pm/\mu\varepsilon]$	0.0096	0.0243	0.0262
K_{T}^{diff} $[pm/°C]$	-0.467	-1.080	-1.071

Mechanical calibration was conducted at a constant temperature of 30 $°C$ to isolate mechanical strain effects from thermal ones. The results display linear behavior and high repeatability across cycles, confirming the reliability of the procedure (Figure 16).

Thermal sensitivity characterization was conducted through three tests in which the optical fiber was held under zero-strain conditions. Each test included both heating and cooling cycles (Figure 17).

At low temperatures, below 40 $°C$, a slight deviation from linearity was observed. This phenomenon is also reported by (Ref. 22) and appears to be related to the material itself rather than its geometry or coating.

After the calibration of the fiber-optic sensors, two mechanical verification cycles were conducted. The first cycle was performed at a constant temperature of -5 $°C$, while the second cycle was carried out at 75 $°C$. It is important to note that the stress values were applied in a random and non-monotonic order. Additionally, the strain values differed among the sensors and were selected within the individual calibration range of each sensor. Specifically, the first sensor was tested with 14 strain levels up to a maximum of 8000 $\mu\varepsilon$, the second with 13 levels up to 6000 $\mu\varepsilon$ and the third with 11 levels up to 2500 $\mu\varepsilon$.

Table 7. Distribution of residuals for tests with constant temperature and variable strain.

	Variable Strain (75 $°C$)	Variable Strain (-5 $°C$)
MK2	-35.80 $\pm$ 50.93 $\mu\varepsilon$	-50.43 $\pm$ 49.89 $\mu\varepsilon$
	5.89 $\pm$ 5.88 $°C$	4.84 $\pm$ 10.13 $°C$
MK3-S1	-12.68 $\pm$ 97.20 $\mu\varepsilon$	63.21 $\pm$ 64.25 $\mu\varepsilon$
	-0.55 $\pm$ 9.48 $°C$	-9.49 $\pm$ 6.26 $°C$
MK3-S2	-63.67 $\pm$ 67.29 $\mu\varepsilon$	-90.99 $\pm$ 35.91 $\mu\varepsilon$
	3.76 $\pm$ 7.02 $°C$	5.51 $\pm$ 3.96 $°C$

For the thermal verification, a single cycle was performed. This cycle was conducted at constant strain levels of 4000 $\mu\varepsilon$, 5000 $\mu\varepsilon$ and 1800 $\mu\varepsilon$ for the MK2 sensor, MK3-S1 sensor and MK3-S2 sensor, respectively. At these fixed strain levels, 11 temperature points were tested within the range of -10 $°C$ to 100 $°C$.

For the mixed tests (Figure 18, 19 and 20), in which only one external stimulus was varied while the other remained constant, the residual distributions were calculated in terms of mean and standard deviation. The results for tests conducted at constant temperature with variable strain are reported in Table 7, while those for tests at constant strain with variable temperature are presented in Table 8.

Table 8. Distribution of residuals for tests with constant strain and variable temperature.

	Variable Temperature (Constant Strain)
MK2	-102.72 ± 97.73 $\mu\varepsilon$
	9.49 ± 9.30 $°C$
MK3-S1	18.09 ± 98.76 $\mu\varepsilon$
	-3.05 ± 10.71 $°C$
MK3-S2	-28.40 ± 45.11 $\mu\varepsilon$
	1.11 ± 4.08 $°C$

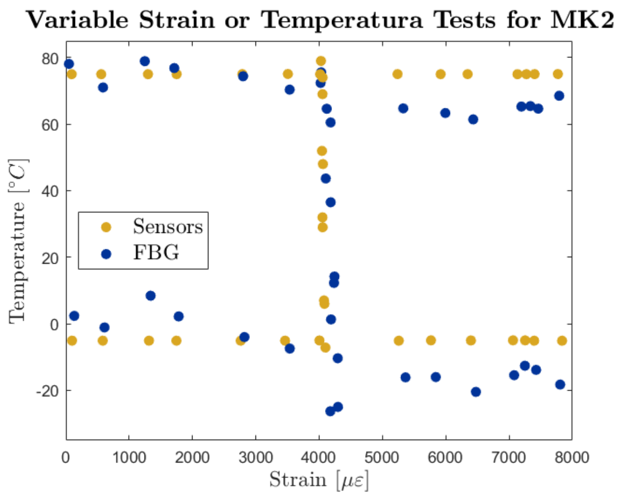

Figure 18. Difference between measured value with sensors and calculated value with FBG for MK2 sensor changing strain at constant temperature and vice versa.

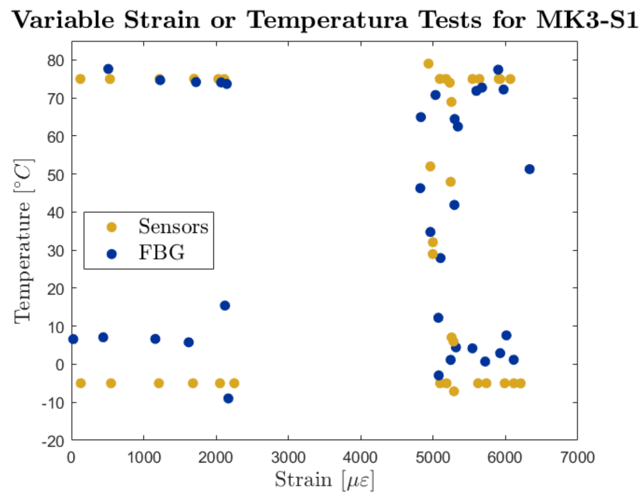

Figure 19. Difference between measured value with sensors and calculated value with FBG for MK3-S1 sensor changing strain at constant temperature and vice versa.

Table 9. Numerical–experimental comparison after optimization process for determining physical parameters of FE model.

	Experimental	Simulation
$E\ [MPa]$	32382.55	32416.81
Peak Distance $[nm]$	0.3343	0.3924
$K_T^{diff}\ [pm/°C]$	-0.467	-0.405
$K_\varepsilon^{diff}\ [pm/\mu\varepsilon]$	0.009648	0.009646

Numerical Model

The thermal-loading simulation began by assigning every mesh node an initial temperature equal to 1000 $°C$ and then constraining the geometry so that, as the entire mesh was uniformly cooled to 20 $°C$, the resulting thermal-shrinkage stresses could develop. The computed stress magnitudes and distributions (Figure 21 and 22) were found to lie within the range reported in the literature (Ref. 21), confirming the validity of this procedure.

Building on this validation, the model's material parameters were calibrated through an optimization process to match those of the fiber used in the experiments, while the geometry was kept unchanged. Section *Materials and Methods - Numerical Model* provides details of the calibration procedure and Table 9 presents a comparison between the physical parameters obtained from the simulation and those measured experimentally. The relative errors are 0.11% for the Young's modulus, 17.37% for the peak distance, 13.31% for the thermal sensitivity and 0.02% for the mechanical sensitivity.

Following the calibration of the fiber model, composite panel simulations were carried out to investigate the influence of fiber embedment on sensor sensitivity. Six simulations were performed to evaluate both mechanical and thermal behavior, considering three fiber orientations relative to the composite section: 0°, 45° and 90°. The 0° orientation corresponds to SAP elements aligned with the longer edge of the composite, while the 90° orientation aligns them with the shorter edge. In all cases, the residual stresses from the fiber cooling simulation were imported as initial conditions. The loading conditions included a 2% applied strain and a temperature range from 30 $°C$ to 130$°C$. Thermal and mechanical sensitivity trends were determined using the same procedure described in Section *Materials and Methods - Numerical Model*. The resulting sensitivities are reported Figure 23 and 24.

Table 10. Nominal wavelengths of FBG sensors in birefringent fibers after embedment in composite material specimens.

	$\lambda_{fast}\ [nm]$	$\lambda_{slow}\ [nm]$	$\delta\lambda\ [nm]$
MK2	1549.513	1549.855	0.3419
MK3-S1	1515.061	1515.863	0.8020
MK3-S2	1520.989	1521.694	0.7050

Experimental Validation and Testing

During the experimental phase, specimens were manufactured with embedded fibers and thermocouples, as described in Section *Materials and Methods - Experimental Validation and Testing*. Prior to calibrating the sensors after embedment, new reference peak wavelengths were measured at zero strain and ambient temperature to enable comparison with the pre-embedment values. These updated nominal values are reported in Table 10.

By comparing the results in Table 10 with those of the unembedded fibers in Table 1, a reduction in peak distance of 0.87% was observed for the MK2, 0.16% for the MK3-S1 and 10.99% for the MK3-S2. Furthermore, the fast peak wavelengths revealed a decrease of 0.02% for the MK2, negligible variation for the MK3-S1 and an increase of 0.8% for the MK3-S2.

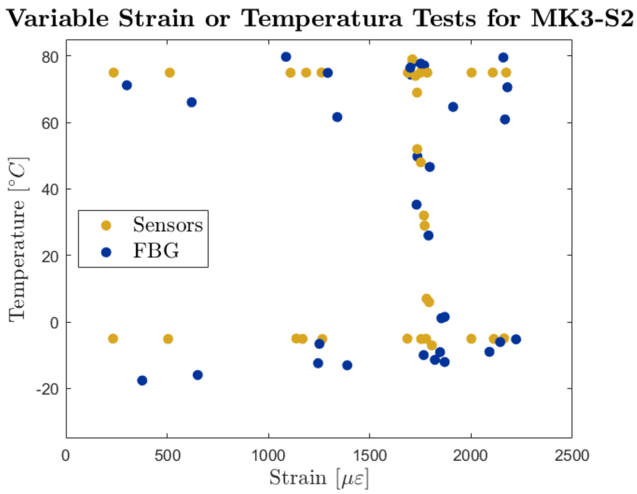

Figure 20. Difference between measured value with sensors and calculated value with FBG for MK3-S2 sensor changing strain at constant temperature and vice versa.

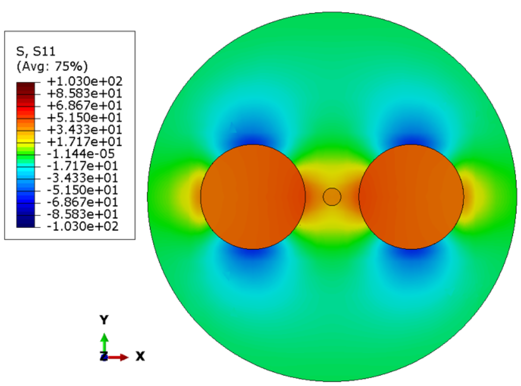

Figure 21. Internal stress distribution S_{11} of a Panda fiber at ambient temperature without applied strain.

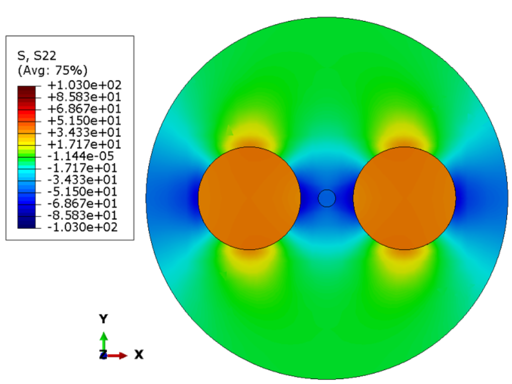

Figure 22. Internal stress distribution S_{22} of a Panda fiber at ambient temperature without applied strain.

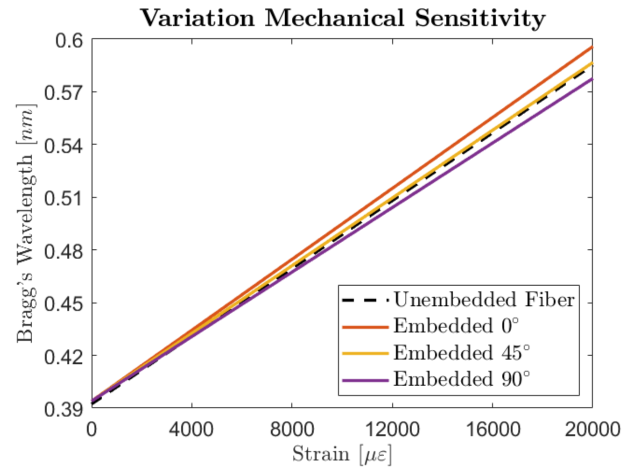

Figure 23. Finite element simulation of variation in mechanical sensitivity as function of fiber embedment angle within composite specimen.

Table 11. Mechanical and thermal sensitivity of fast peak and peak separation for embedded FBG in composite speciment inscribed in Panda birefringent fiber by AtGrating (MK2), in Bow-tie birefringent fiber by FBGS (MK3-S1) and in Bow-tie birefringent fiber by FBGS (MK3-S2).

	MK2	MK3-S1	MK3-S2
K_{ε}^{fast} $[pm/\mu\varepsilon]$	1.203	1.229	1.166
K_{T}^{fast} $[pm/°C]$	14.748	16.020	15.117
K_{ε}^{diff} $[pm/\mu\varepsilon]$	0.0087	0.0220	0.0205
K_{T}^{diff} $[pm/°C]$	-0.5234	-0.7991	0.2073

Mechanical calibration was performed using an MTS 810 Material Test System. For each specimen, the calibration was carried out using the same maximum strain level applied during the unembedded fiber tests. The tests were conducted under a constant strain rate of 25 $\mu\varepsilon/s$, with continuous acquisition from the FBG interrogator. For the MK2 and MK3-S2, the calibration was repeated three times. In contrast, only one test was performed on MK3-S1 due to significant oscillations in peak intensity, which made it difficult to complete multiple reliable repetitions (Figure 25).

The MK2 and MK3-S1 sensors were calibrated using a Memmert Universal Oven UF110plus. Thermal calibration was repeated three times, with a maximum temperature of 100 $°C$. For both, the thermal cycles were applied at a controlled heating/cooling rate of 2 $°C/min$, with continuous data acquisition from the FBG sensors throughout the tests. The thermal calibration of the MK3-S2 sensor was performed using infrared heating, with temperature monitored via the embedded thermocouple. This sensor was tested only once, up to a maximum temperature of 45 $°C$, due to optical fiber failure that prevented further testing (Figure 26).

All embedded sensors showed a decrease in mechanical sensitivity compared to the non-embedded reference sensors, with

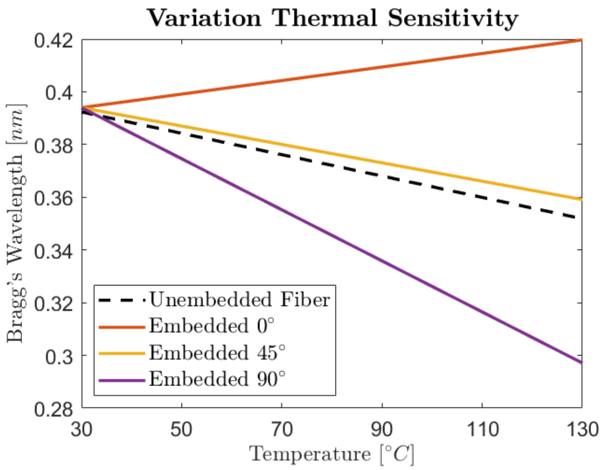

Figure 24. Finite element simulation of variation in thermal sensitivity as function of fiber embedment angle within composite specimen.

reductions of 4.82%, 1.68% and 7.75% for the MK2, MK3-S1 and MK3-S2, respectively. Similarly, the peak separation under mechanical loading maintained a linear trend, although with increased dispersion relative to the fast peak behavior, and showed sensitivity reductions of 10.01%, 9.65% and 21.65% for the same three sensors.

In contrast, thermal calibration revealed an increase in sensitivity for all embedded sensors when compared to their non-embedded counterparts. Specifically, thermal sensitivity increased by 30.61% for the MK2, 24.36% for MK3-S1 and 16.04% for MK3-S2. The peak separation response under thermal loading remained linear but displayed higher variability. Notably, the peak separation sensitivity increased by 11.98% for the MK2, while it decreased significantly for the FBGS sensors: -25.97% for MK3-S1 and -119.36% for MK3-S2. These results confirm the impact of embedding and fiber type on the performance and reliability of FBG sensors in composite applications.

To validate the calibration of the embedded optical fiber sensors, a combined thermal and mechanical loading cycles was performed (Figure 27). Due to physical constraints, this test was conducted only on specimens with the AtGrating (MK2). The test setup, MTS 810 Material Test System, was modified with the addition of infrared lamps to control specimen temperature. The strain response of the AtGrating sensor closely followed the applied loading, whereas the temperature signal remained consistent during loading. From this test, the distributions of residuals of the AtGrating sensor were estimated as -53.92 ± 54.14 $\mu\varepsilon$ for strain and -6.52 ± 6.46 °C for temperature.

Finally, the orientation angle of the embedded optical fibers was assessed to establish the relationship between sensitivity variations and embedment angle. Specimens were sectioned adjacent to each sensor, embedded in thermosetting resin, and polished prior to SEM imaging. The MK3-S1 sensor exhibited an embedment angle of 61° (Figure 28) and the MK3-S2 sensor of 1° (Figure 29).

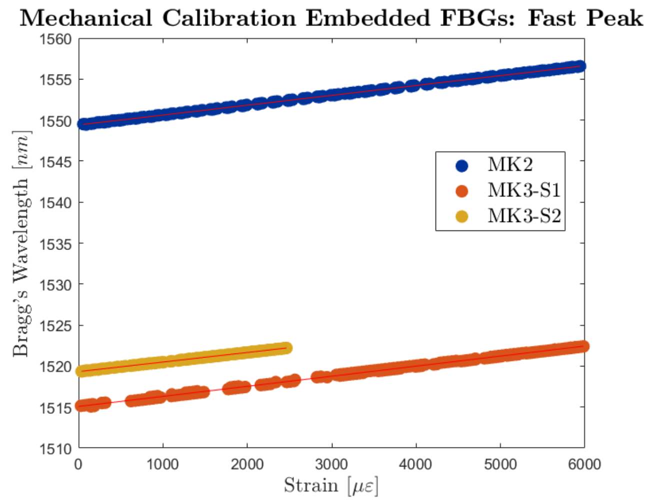

Figure 25. Mechanical calibration of FBGs embedded within composite material specimens. Details of fast peak.

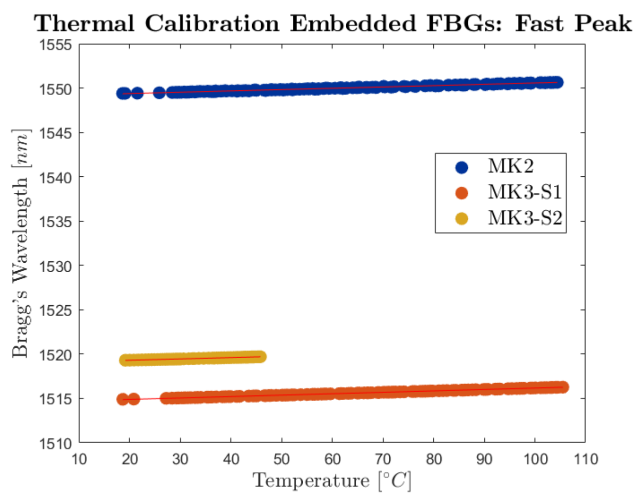

Figure 26. Thermal calibration of FBGs embedded within composite material specimens. Details of fast peak.

For the MK2 sensor, it was not possible to directly measure the fiber orientation. Due to the poor adhesion of the acrylate coating and its glass transition temperature being incompatible with the curing cycle, the fiber cross-section did not remain flat during sample preparation. As a result, the brittle glass fiber fractured during polishing, preventing visualization of the Panda fiber cross-section (Figure 30). However, the embedment angle was inferred to lie between 45° and 61°, as this is the only range for which the observed decrease in strain sensitivity and increase in temperature sensitivity are consistent with the FE model predictions.

DISCUSSION

In this study, and more generally for the investigation of FBG sensor behavior, a dedicated experimental setup was developed to enable accurate thermo-mechanical calibration and

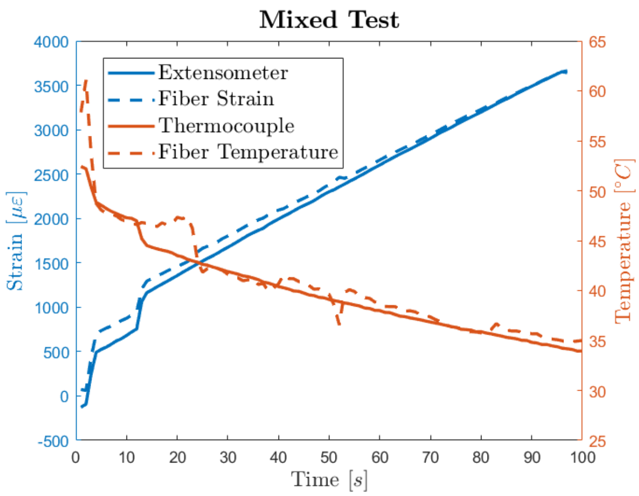

Figure 27. Tests on embedded MK2 sensor under varying temperature and strain.

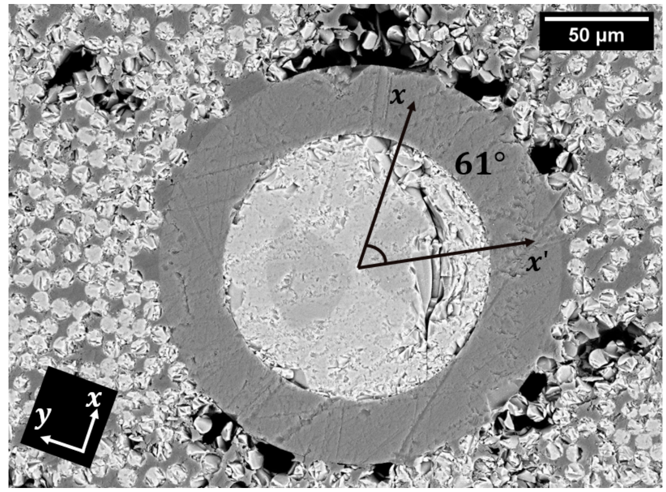

Figure 28. Schematic of embedding angle in MK3-S1 composite sensor specimen. Global specimen coordinate system x–y is defined with x along specimen width and y through its thickness. Local fiber-section coordinate system x'–y'.

testing. The system was designed to operate over a wide range of temperatures, from sub-zero conditions ($-19.62\ °C$) to well above 100 $°C$ (up to 131.58 $°C$), and to apply mechanical strain levels up to 8000 $\mu\varepsilon$. To achieve these performance targets, specific efforts were made to enhance thermal stability, prevent fiber slippage and minimize the risk of fiber breakage during loading.

To ensure accurate strain evaluation, the calibration adopted a force-to-strain conversion approach based on load cell measurements and the force-strain conversion coefficient, which are less affected by hysteresis compared to direct strain measurements using capstans. The coefficients were obtained from mechanical tests performed at constant temperature and under low strain levels, without the use of capstans (approximately 2000 $\mu\varepsilon$ and 1.8 N). Calibration at higher strain levels, however, requires the use of capstans to prevent fiber breakage near the gripping area, where stress concentrations are more likely to occur.

The experimental campaign has begun with the calibration of three different sensors to determine their sensitivities. One sensor, manufactured by AtGrating, was based on a commercial acrylate-coated Panda fiber, which, while more economical, is not optimized for sensing applications and thus offers lower performance. The other two sensors were fabricated by FBGS and inscribed on an Ormocer-coated Bow-Tie fiber specifically designed for sensing purposes. This specialized fiber increases the birefringence, resulting in improved sensing capabilities. As part of the calibration procedure, nominal values for peak separation and fast-axis wavelength were obtained under controlled conditions: at 30 $°C$ and without the application of mechanical strain. Analysis of the spectral data showed that the FBGS fibers exhibited a larger separation between the fast and slow polarization peaks compared to the AtGrating fiber, consistent with their higher birefringence. Although the AtGrating sensor presented less baseline noise, it required a lower gain to reach the target optical power of 3000 AU, compared to the FBGS sensors. The data collection from each sensor confirmed that the FBGS fibers provided higher birefringence, which is beneficial for enhanced sensing resolution.

The mechanical calibration procedure involved repeated loading–unloading cycles, which revealed a highly linear and repeatable response as a function of applied strain. Figure 16 illustrates the strong linear behavior of the fast peak wavelength for all three sensors. Regarding the peak separation, it was observed that reducing the maximum strain while maintaining eight measurement points per cycle introduced greater difficulty in managing the calibration setup. As a result, although the overall trend remained linear, increased signal oscillations were evident. In this study, the peak separation was also considered to vary linearly with strain. However, a more detailed investigation into the relationship between birefringence, and therefore peak separation, and the stress state of the fiber will be pursued in future work. Additionally, the results showed that sensors with higher nominal wavelengths exhibited greater mechanical sensitivity in the fast peak response. Conversely, the peak separation sensitivity was found to be higher in the FBGS sensors, which can be attributed to the greater intrinsic birefringence of the fiber used.

The thermal calibration was carried out under zero-stress conditions to isolate the effects of temperature on the optical response of the sensors. The results showed that above 40 $°C$, the fast peak wavelength exhibited a clear linear trend with high repeatability across all cycles and sensors. However, below this threshold, deviations from linearity were observed, more evident in the FBGS sensors due to their higher birefringence and thermal sensitivity. This consistent nonlinearity across all sensors suggests the presence of an underlying physical phenomenon within the fiber material. In support of this, a model from the literature describing the temperature dependence of the refractive index predicts non-linear behav-

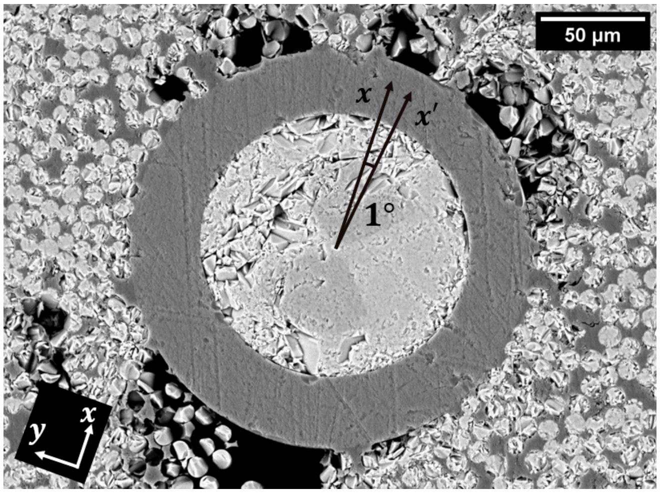

Figure 29. Schematic of embedding angle in MK3-S2 composite sensor specimen. Global specimen coordinate system x–y is defined with x along specimen width and y through its thickness. Local fiber-section coordinate system x'–y'.

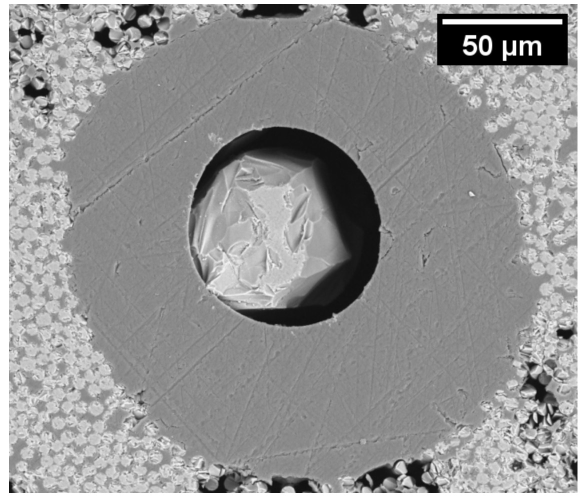

Figure 30. MK2 fiber embedded in composite specimen. Poor adhesion properties of coating and polishing process prevent visualization of fiber cross-section.

ior below 40 $°C$, which aligns with the experimental data. While the peak separation also displayed an overall linear trend with temperature, it was more susceptible to oscillations compared to the fast peak wavelength. The FBGS sensors demonstrated higher thermal sensitivity in both parameters, consistent with their greater birefringence. Moreover, within the FBGS group, the thermal sensitivity increased with nominal wavelength.

Regarding the combined tests at constant temperature and variable strain, the most evident observation is the performance difference between low- and high-temperature tests, with the latter yielding more accurate and consistent results. This discrepancy can be attributed to the nonlinear thermal behavior discussed previously, particularly at temperatures below 40 $°C$. Among the high-temperature tests, the best performance was achieved by the first sensor of the FBGS chain, which benefits from both a higher birefringence and a mechanical calibration that effectively utilized the full available strain range. The second-best performance was obtained from the AtGrating sensor, which, despite having lower birefringence compared to the second FBGS sensor, demonstrated superior mechanical calibration. In contrast, the second FBGS sensor exhibited comparatively lower accuracy, highlighting the importance of fully exploiting the experimental setup during calibration, especially in terms of strain range.

For the thermal verification under constant strain, the sensors inscribed in the FBGS fiber outperformed the AtGrating sensor, owing to their higher birefringence and, consequently, greater sensitivity to temperature variations. Notably, both FBGS sensors yielded comparable results in this test configuration, suggesting consistent thermal behavior within the same fiber type.

It is important to note that the constant-temperature tests were conducted at the same thermal condition for all sensors but with varying levels of applied strain, whereas the constant-strain thermal tests were performed over the same temperature range but at different fixed strain levels. These differences in testing conditions significantly influenced the accuracy of the resulting sensitivity coefficients. In particular, sensitivities obtained at lower strain levels were less reliable than those derived from tests at high strain levels that exploited the full mechanical range of the sensor.

Overall, the calibration and testing campaign provided valuable insight into the performance of the different fiber sensors and the effectiveness of the calibration procedures. To enhance accuracy, it is essential to maximize the use of the full strain range during mechanical calibration, acquiring sufficient data points across both low and high strain levels. Similarly, thermal calibration should cover the complete temperature range, with a focus on increasing the number of data points at lower temperatures, where greater deviations from the linearity were observed. Additionally, repeating both thermal and mechanical calibration cycles is crucial to minimize the influence of testing machine errors on the calibration coefficients and ensure reproducibility and robustness of the calibration results.

To investigate the influence of the embedding angle of optical fiber cross-sections within composite materials, a numerical model was developed to simulate the stress-induced birefringence in the embedded fibers. The simulation results showed good agreement with findings reported in the literature, confirming the validity of the modeling approach. Based on this, the model was specifically adapted to the Panda fiber used in the experimental campaign. The geometrical parameters of the fiber were obtained through SEM, while the physical parameters were identified through an optimization process aimed at matching the model response with experimental data. This enabled the creation of a Digital Twin of the fiber, capable of predicting variations in sensitivity due to the embedding conditions.

The simulations demonstrated that the orientation of the embedded fiber significantly affects its thermal and mechanical sensitivities. In particular, a 90° orientation increases thermal sensitivity, while 45° causes only minor changes and 0° not only reduces sensitivity but can also invert the trend of peak separation with temperature. Conversely, for mechanical sensitivity, the trend is reversed: the 0° orientation improves sensitivity, while the 90° orientation reduces it. The results obtained from the numerical simulations in ABAQUS indicate that no single orientation simultaneously optimizes both thermal and mechanical sensitivity. This effect can be used to increase one of the two sensitivities. However, the 45° orientation introduces only minimal deviations compared to the unembedded configuration, suggesting it could serve as a compromise, reducing the extent of additional calibration required for embedded sensing applications. The orientation of the fiber section within the composite can thus enhance one sensitivity over the other.

The numerical results were subsequently validated through experimental testing on the embedded fibers. Following the embedding process, the nominal values of the fast peak wavelength and the peak separation were re-evaluated under ambient temperature and zero strain conditions. A comparison between the embedded and non-embedded configurations revealed changes in both parameters. Specifically, the peak separation decreased by 0.87% for the AtGrating sensor, by 0.16% for the first FBGS sensor and by 10.99% for the second FBGS sensor. In terms of the fast peak wavelength, a decrease of 0.02% was observed for the AtGrating sensor, a negligible change for the first FBGS sensor and an increase of 0.8% for the second FBGS sensor.

Mechanical calibration of the embedded fibers showed that all three sensors retained a linear response in the fast peak wavelength as a function of strain. However, a reduction in sensitivity was observed when compared to the non-embedded condition. Specifically, the sensitivity decreased by 4.82% for the AtGrating sensor, 1.68% for the first FBGS sensor and 7.75% for the second FBGS sensor. For the peak separation, although a linear trend was still present, the data exhibited greater dispersion. Sensitivity reductions of 10.01%, 9.65% and 21.65% were observed for the AtGrating, first FBGS and second FBGS sensors, respectively. These results confirm that mechanical embedding alters the fiber's response, likely due to stress redistribution and constraints imposed by the host material.

Thermal calibration of the embedded sensors also yielded a linear behavior in the fast peak wavelength across all three fibers. In contrast to the mechanical case, thermal sensitivities increased after embedding. Specifically, the AtGrating, first FBGS and second FBGS sensors exhibited sensitivity increases of 30.61%, 24.36% and 16.04%, respectively, relative to their non-embedded counterparts. For the peak separation, the AtGrating sensor showed an 11.98% increase in sensitivity, while the two FBGS sensors exhibited significant reductions of 25.97% and 119.36%, respectively. These contrasting behaviors between mechanical and thermal responses highlight the complex interaction between fiber geometry, embedding orientation and the surrounding matrix.

The AtGrating sensor was ultimately used to evaluate the actual decoupling capability of the FBG sensing system. As demonstrated, the sensor accurately tracked the applied strain on the specimen while simultaneously providing reliable temperature measurements, confirming its potential for dual-parameter sensing. However, further studies are necessary to determine whether the sensor can maintain this decoupling performance under rapid or simultaneous changes in strain and temperature. Moreover, due to limitations during testing, the decoupling capability of the other two FBGS sensors could not be assessed. Given the significant changes observed in their sensitivities post-embedding, particularly for the MK3-S2 sensor, it would be essential to fabricate new composite samples using these fibers in order to fully evaluate their performance in real operating conditions.

To determine the actual embedding angle of the optical fibers after composite manufacturing, the specimens were sectioned near the FBG sensors and analyzed using SEM. This analysis enabled a direct evaluation of the sensor orientation, which was then correlated with the variations in calibration and validation results post-embedding. The first FBGS sensor, embedded at an angle of 61°, exhibited a reduction in both its peak distance sensitivity to strain and to temperature. Similarly, the fast peak wavelength sensitivity decreased for strain and increased for temperature. The second FBGS sensor, embedded at an angle of 1°, showed an even more pronounced reduction in both peak distance sensitivities. This behavior was not anticipated by the FEM simulations, which predicted that it would not be possible to simultaneously reduce both thermal and mechanical sensitivities. This discrepancy is attributed to the fact that the model was developed for a Panda-type fiber (AtGrating), while the FBGS sensors are inscribed on Bow-tie fibers with different internal geometries. These structural differences likely affect the stress distribution and resulting birefringence, thus requiring the development of a dedicated FEM model for Bow-tie fibers to obtain accurate predictive capabilities.

The current embedment process is highly sensitive to manual execution, particularly due to the method used to apply lateral force via a suspended weight. Small variations in the position or alignment of this weight can lead to significant errors in sensor placement, which may account for the incorrect orientation observed in one of the samples. Additionally, the fiber rotation mechanism, based on wheels with an angular resolution of 6°, lacks the precision required for accurate control of the embedding angle. To enable more reliable and repeatable studies on the influence of fiber orientation after embedding, both the force application system and angular adjustment accuracy must be improved.

For the AtGrating sensor, it was not possible to determine the orientation directly due to the weak adhesion between the acrylate coating and the glass cladding. This poor bonding, resulting from the coating's glass transition temperature (T_g) lower than the composite curing temperature, caused the cladding to detach during specimen preparation. The SEM image highlights these limitations, showing that the fiber does not remain properly embedded in the coating and that the original circular geometry of the coating is significantly deformed.

Nonetheless, based on the variation in peak distance and similarity to the first FBGS sensor, it is reasonable to assume that the AtGrating sensor was embedded at an angle between 45° and 61°. This orientation range is also supported by the embedding procedure adopted, which aimed to minimize sensitivity changes. Post-embedding results for the AtGrating sensor showed a decrease in peak distance sensitivity to strain and an increase in sensitivity to temperature, trends that match those predicted by the FEM model for fibers embedded within this angular range. Furthermore, the fast peak wavelength sensitivity decreased for strain and increased for temperature, again consistent with model expectations. Importantly, the overall sensor accuracy remained largely unaffected, in contrast to the FBGS sensors.

In conclusion, the AtGrating sensor experienced the smallest sensitivity deviations upon embedding, maintaining reliable performance. These results confirm the validity of the numerical-experimental approach adopted to estimate the fiber embedding angle during composite lamination. While the FEM model demonstrated good predictive capability for Panda-type fibers, the differences observed with Bow-tie fibers underline the necessity of developing a specific numerical model to accurately describe their behavior in embedded configurations.

CONCLUSIONS

1. A custom calibration setup was designed and validated, enabling accurate calibration of FBG sensors over extended temperature and strain ranges.

2. Calibration procedures using both fast peak shift and peak distance variation allowed for the decoupling of strain and temperature effects, achieving a discrimination efficiency of approximately 10%, in line with or better than values reported in the literature.

3. The best FBGS sensor achieved a temperature distribution of residuals of -0.55 ± 9.48 $°C$ and of -12.68 ± 97.20 $\mu\varepsilon$ for strain, confirming the potential of the method when properly calibrated.

4. A finite element model, optimized for the AtGrating Panda fiber, accurately predicted changes in mechanical and thermal sensitivities due to embedding and orientation effects.

5. Experimental embedding of FBG sensors confirmed that fiber orientation significantly affects performance. The AtGrating sensor, embedded at 45$°C$–61$°C$, maintained performance close to the non-embedded case, validating the model predictions.

6. The second FBGS sensor, embedded at 1$°C$, lost the ability to decouple strain and temperature due to a significant drop in sensitivity and signal reliability.

7. SEM analysis of the AtGrating sensor revealed poor adhesion between the acrylate coating and fiber cladding due to a T_g below the curing temperature, leading to coating deformation and detachment.

8. The current FEM model, based on a Panda geometry, could not predict the behavior of Bow-tie FBGS fibers. A dedicated model is required to account for their distinct internal structure.

9. The combined numerical-experimental methodology proved effective in estimating the fiber embedding angle during lamination, supporting its use for controlled sensor integration in composites.

Author contact:
Emanuele Casciaro, emanuele.casciaro@polimi.it,
Diego Henriquet, diego.henriquet@mail.polimi.it,
Andrea Baldi, andrea.baldi01@leonardo.com,
Paolo Bettini, paolo.bettini@polimi.it.

ACKNOWLEDGMENTS

This research has been supported by ASI (Italian Space Agency), grant agreement 2018-5-HH.0.

Funded by the European Union- Next Generation EU, Mission 4 Component 1 CUP D43C23002190008.

REFERENCES

1. Sala, G., Landro, L. D., Airoldi, A., and Bettini, P., "Fibre optics health monitoring for aeronautical applications," *Meccanica*, Vol. 50, (10), Oct. 2015, pp. 2547–2567. DOI: 10.1007/s11012-015-0200-6.

2. Sante, R. D., "Fibre Optic Sensors for Structural Health Monitoring of Aircraft Composite Structures: Recent Advances and Applications," *Sensors*, Vol. 15, (8), 2015, pp. 18666–18713. DOI: 10.3390/s150818666.

3. Kersey, A. D., Davis, M. A., Patrick, H., LeBlanc, M., Koo, K., Askins, C., Putnam, M., and Friebele, E., "Fiber grating sensors," *Journal of Lightwave Technology*, Vol. 15, (8), 1997, pp. 1442–1463.

4. Hill, K. O., and Meltz, G., "Fiber Bragg grating technology fundamentals and overview," *Journal of Lightwave Technology*, Vol. 15, (8), 1997, pp. 1263–1276.

5. Jung, D.-W., Kwon, I.-B., and Choi, N.-S., "Application of a Temperature-Compensating FBG Sensor to Strain Measurement," *Advanced Materials Research*, Vol. 26-28, 2007, pp. 1089–1092. DOI: 10.4028/www.scientific.net/AMR.26-28.1089.

6. Zhou, Z., and Ou, J., "Techniques of temperature compensation for FBG strain sensors used in long-term structural monitoring," Proceedings of SPIE - The International Society for Optical Engineering, Vol. 5851, 2005. DOI: 10.1117/12.634047.

7. Triollet, S., Robert, L., Marin, E., and Ouerdane, Y., "Discriminated measures of strain and temperature in metallic specimen with embedded superimposed long and short fibre Bragg gratings," *Measurement Science and Technology*, Vol. 22, (1), 2011, pp. 015202. DOI: 10.1088/0957-0233/22/1/015202.

8. Hu, Q., Wang, P., Rao, B., Wang, M., Wang, Z., and Xu, X., "Simultaneous measurement of temperature and strain using double-cladding fiber based hybrid Bragg grating," *OSA Continuum*, Vol. 3, (4), 2020, pp. 1031–1037. DOI: 10.1364/OSAC.389645.

9. Kang, Z., Sun, J., Bai, Y., and Jian, S., "Twin-Core Fiber-Based Erbium-Doped Fiber Laser Sensor for Decoupling Measurement of Temperature and Strain," *IEEE Sensors Journal*, Vol. 15, (7), 2015, pp. 6828–6832. DOI: 10.1109/JSEN.2015.2460731.

10. Jiang, J., Wang, X., Liu, T., Jiang, D., Qiu, K., and Wang, Y., "Multi-Parameter Sensing Using a Fiber Bragg Grating Inscribed in Dual-Mode Fiber," *IEEE Photonics Technology Letters*, Vol. 29, (20), 2017, pp. 1716–1719. DOI: 10.1109/LPT.2017.2737013.

11. Pereira, G. F., McGugan, M., and Mikkelsen, L. P., "Method for independent strain and temperature measurement in polymeric tensile test specimen using embedded FBG sensors," *Polymer Testing*, Vol. 50, 2016, pp. 125–134. DOI: 10.1016/j.polymertesting.2016.01.005.

12. Wang, C., Huang, Z., Li, G., Zhang, S., Zhao, J., Zhao, N., Cai, H., and Zhang, Y., "Simultaneous Temperature and Strain Measurements Using Polarization-Maintaining Few-Mode Bragg Gratings," *Sensors*, Vol. 19, (23), 2019, pp. 5221. DOI: 10.3390/s19235221.

13. Oh, S.-T., Han, W.-T., Paek, U.-C., and Chung, Y.-I., "Discrimination of temperature and strain with a single FBG based on the birefringence effect," *Optics Express*, Vol. 12, (4), 2004, pp. 724–729. DOI: 10.1364/OPEX.12.000724.

14. Casciaro, E., Rigamonti, D., and Bettini, P., "Birefringent optical fibers to decouple thermo-mechanical effects on FBG sensors," Proceedings of the 11th European Workshop on Structural Health Monitoring (EWSHM 2024), Licensed under CC BY 4.0, 2024.

15. Casciaro, E., Scalia, T., Albano, M., and Bettini, P., "SHM of Space Structures: Use of Polarization-Maintaining Fibers to Decouple the Thermo-Mechanical Effect on Fiber Bragg Grating Sensor Measurements," 75th International Astronautical Congress (IAC), October 2024.

16. Wang, Y., Han, B., Kim, D. W., Bar-Cohen, A., and Joseph, P., "Integrated measurement technique for curing process-dependent mechanical properties of polymeric materials using fiber Bragg grating," *Experimental Mechanics*, Vol. 48, (1), 2008, pp. 107–117. DOI: 10.1007/s11340-007-9067-3.

17. Becker, R. A., *Introduction to Theoretical Mechanics*, McGraw-Hill Book Company, Inc., New York, Toronto, London, 1954.

18. Guan, R., Zhu, F., Gan, Z., Huang, D., and Liu, S., "Stress birefringence analysis of polarization maintaining optical fibers," *Optical Fiber Technology*, Vol. 11, (2), 2005, pp. 240–254. DOI: 10.1016/j.yofte.2004.10.002.

19. Gafsi, R., and Sherif, M. A. E., "Analysis of induced-Birefringence effects on fiber Bragg gratings," *Optical Fiber Technology*, Vol. 6, (3), 2000, pp. 299–323.

20. Tsai, K.-H., Kim, K.-S., and Morse, T. F., "General solutions for stress-induced polarization in optical fibers," *Journal of Lightwave Technology*, Vol. 9, (1), 1991, pp. 7–17.

21. Annunziato, A., Anelli, F., Gates, J., Holmes, C., and Prudenzano, F., "Design of Polarization-Maintaining FBGs Using Polyimide Films to Improve Strain-Temperature Sensing in CFRP Laminates," *IEEE Photonics Journal*, Vol. 13, (2), 2021, pp. 7100315. DOI: 10.1109/JPHOT.2021.3063172.

22. Tan, C., and Arndt, J., "Temperature dependence of refractive index of glassy SiO_2 in the infrared wavelength range," *Journal of Physics and Chemistry of Solids*, Vol. 61, (8), 2000, pp. 1315–1320. DOI: 10.1016/S0022-3697(99)00411-4.